Editors' Suggestion Featured in Physics

Electronegative metal dopants improve switching variability in Al_2O_3 resistive switching devices

Zheng Jie Tan,[1,*] Vrindaa Somjit,[1,*] Cigdem Toparli,[2] Bilge Yildiz,[1,2,†] and Nicholas Fang[3,‡]

[1]Department of Materials Science and Engineering, Massachusetts Institute of Technology (MIT), Cambridge, Massachusetts 02139, USA
[2]Department of Nuclear Science and Engineering, Massachusetts Institute of Technology (MIT), Cambridge, Massachusetts 02139, USA
[3]Department of Mechanical Engineering, Massachusetts Institute of Technology (MIT), Cambridge, Massachusetts 02139, USA

(Received 25 April 2022; revised 28 July 2022; accepted 12 August 2022; published 19 October 2022)

Resistive random-access memories are promising for nonvolatile memory and brain-inspired computing applications. High variability and low yield of these devices are key drawbacks hindering reliable training of physical neural networks. In this paper, we show that doping an oxide electrolyte, Al_2O_3, with electronegative metals makes resistive switching significantly more reproducible, surpassing the reproducibility requirements for obtaining reliable hardware neuromorphic circuits. Based on density functional theory calculations, the underlying mechanism is hypothesized to be the ease of creating oxygen vacancies in the vicinity of electronegative dopants due to the capture of the associated electrons by dopant midgap states and the weakening of Al-O bonds. These oxygen vacancies and vacancy clusters also bind significantly to the dopant, thereby serving as preferential sites and building blocks in the formation of conducting paths. We validate this theory experimentally by implanting different dopants over a range of electronegativities in devices made of multiple alternating layers of Al_2O_3 and WN and find superior repeatability and yield with highly electronegative metals, Au, Pt, and Pd. These devices also exhibit a gradual SET transition, enabling multibit switching that is desirable for analog computing.

DOI: 10.1103/PhysRevMaterials.6.105002

I. INTRODUCTION

Compact and energy-efficient solid-state resistive switching devices are actively being investigated as fundamental units for use as high-density nonvolatile memories and for enabling energy-efficient analog computing via physical neural networks [1–4]. These devices are capable of both data storage and computation, while being scalable to the nanometer regime [5,6]. Such colocation of computing and memory functions in the same unit gives them great promise to circumvent the latency and energy challenge of data movement [1] that plague current computing systems based on von Neumann architecture with separate memory and computing units. One class of such devices is resistive switching random-access memory (RRAM) [7,8], which consists of a metal-insulator-metal stack. The insulating solid electrolyte layer primarily made of chalcogenides or metal oxides becomes the switching medium. The reversible migration and redistribution of metals such as Ag or Cu [9,10] or of defects such as oxygen vacancies (V_O) through the electrolyte under the application of a voltage forms localized, tunable conductive regions that are responsible for switching [2,4,11,12]. The electrical modulation of the electronic conductance in an analog way in such resistive switching units is fundamental to brain-inspired analog computing [13,14].

Two key barriers preventing the widespread use of RRAMs are their high switching variability [5,6,15–19] and poor device yield [11,18,20,21]. These arise due to the inherent stochastic nature of the individual switching events. Variation in the location and the local chemistry and structure of such filaments leads to cycle-to-cycle and device-to-device variations in switching voltages and resistances, causing inconsistent switching [15,16,19,22,23]. In addition, pristine devices typically require an initial electroforming step, in which a voltage much higher than the set voltage is applied to form the first conductive path in the insulating electrolyte [24]. Such large forming biases can sometimes deform and destroy the devices [11,21], resulting in poor device yield. Poor switching repeatability and poor device yield adversely affect device stability, increase peripheral circuit complexity, and importantly, reduce computational accuracy of hardware-implemented neural networks, as highlighted by Gokmen and Vlasov [25] and Li *et al.* [26].

Correspondingly, multiple strategies have been attempted to improve the switching variability and yield of RRAM devices. For example, multilayer structures (such as AlO_x/HfO_x [27,28], TiO_x/Al_2O_3 [29–31], and $HfO_x/TiO_x/HfO_x/TiO_x$ [32]) are thought to enhance switching variability by confining the filament formation and rupture pathways within very thin oxide layers [27–29,32]. Interdiffusion among the oxide layers and potential short circuits across thin films of 1 to 2 nm thickness are limiting factors [29,33] to this approach. Alternatively, nanocrystals [34,35] and nanodots [36] in the electrolyte (such as Ru [34] and Ag [35] nanocrystals in Al_2O_3) enhance the local electric field and preferentially accelerate V_O migration and cation dissolution, thereby reducing the randomness in filament formation, but to fabricate such embedded nanostructures is not trivial or inexpensive.

*These authors contributed equally to this work.
†byildiz@mit.edu
‡nicfang@mit.edu

 ©2022 American Physical Society

Other experiments suggest that introduction of metal dopants [20,37–43] (such as Ge-doped [39] and Al-doped [38,44] HfO_2) into oxide electrolytes improves switching variability. Doping through cosputtering is common, but recent efforts using energetic doping, such as by ion implantation [45], appear to more significantly improve the characters of resistive switching. This is likely due to the modification of the intrinsic defects in the oxide [46] and the different distribution of dopants since cosputtering deposition is frequently affected by island growth. First-principles calculations have suggested that reduced V_O formation energies near the dopant [39,40,42,43,47–49] should increase switching uniformity by localizing the current path. Many of these devices still needed high electroforming voltages [27,29,35,36,40]. Significant variability is still observed [27–29,32,34,38–40], and current compliances [29,34,36,38,40,41,50] are still used. Oxygen vacancy enrichment in an oxide can be achieved by different mechanisms, i.e., aliovalent doping which is charge compensated by oxygen vacancies, or dopants that are easier to reduce than the host oxide under an electrochemical potential. It is important to understand and establish the dopant properties as descriptors for the V_O formation ease and uniformity in the performance of oxide RRAM devices.

In this paper, we hypothesize that dopant electronegativity can be used as a descriptor for predicting the ease of V_O formation in an insulating oxide, with implications for RRAM switching uniformity. Highly electronegative dopants such as Au, Pt, Pd, and Rh on oxides are known to catalyze several important reactions, such as CO oxidation, water-gas shift, and NO reduction [51]. These dopants weaken metal-oxygen bonds in the host oxide lattice [51] while assisting these surface reactions. Following this, we hypothesize that dopants with high electronegativity can give rise to lower switching variability in Al_2O_3 by acting as preferential sites for V_O formation. Highly electronegative dopants reduce the formation energy of oxygen vacancies because they weaken the metal-oxygen bonds and create in-gap states and capture the electrons resulting from neutral oxygen removal (a process that is energetically impossible in undoped Al_2O_3).

In this paper, we combine the above advantages of multilayer thin films and metal dopants to develop a device with superior switching variability and high yield that requires no external control circuitry and is electroforming free. Our original device consists of alternating layers of Al_2O_3 and WN deposited on Si, with the highly electronegative Au as the top electrode material. WN acts as a barrier layer of Al_2O_3 with its lower interdiffusion tendency [52], which is an improvement from previous device configurations [29]. Au atoms were implanted into the Al_2O_3 electrolyte as dopants alongside focused ion beam (FIB) milling while defining the device area. Density functional theory (DFT) calculations revealed a significant lowering of V_O formation energy in the vicinity of Au due to the changes in the electronic structure brought about by the high electronegativity of Au. Thus, cohesive clusters of oxygen vacancies anchored around the electronegative dopants act as the fundamental units that form an extended switchable network. Multilayer devices doped in this way with Au had superior cycle-to-cycle and device-to-device switching variability than the undoped devices, consistent with the prediction of stable conducting paths obtained by the DFT model. Using this as the control device, we focused our study on predicting and experimentally validating that other highly electronegative dopants such as Pt and Pd similarly increase the uniformity of resistive switching among multiple devices and cycles, in contrast to active metals such as Cu, Ti, and Al. Furthermore, our device exhibits a gradual SET transition, which coupled with its high uniformity makes it a favorable candidate for use in multibit switching applications.

II. METHODS

A. Computational

DFT calculations

The energetics of the $2\times2\times1$ perfect supercell ($a = 9.62$ Å, $c = 13.13$ Å) and of all the defects were calculated using DFT using a plane-wave basis set, projector-augmented wave pseudopotentials [53], and the Perdew-Burke-Ernzerhof parameterization of the generalized gradient approximation (GGA) [54] as the exchange-correlation functional, as implemented in the Vienna *Ab initio* Simulation Package [55], v.5.4.1. A kinetic energy cutoff of 520 eV and a γ-centered $2\times2\times2$ k-point mesh was used, resulting in a convergence accuracy of <1 meV/atom. All calculations were performed with a Gaussian smearing width of 0.05 eV and spin-polarized setting. Atomic positions were relaxed until the force on each atom was <0.02 eV/Å.

The formation energy of a neutral oxygen vacancy (V_O) in bulk Al_2O_3 was calculated as

$$E_f = E_{\mathrm{DFT}}^{V_O} - E_{\mathrm{DFT}}^{\mathrm{perf}} + \mu_O, \quad (1)$$

where E_f is the formation energy of V_O in bulk Al_2O_3, $E_{\mathrm{DFT}}^{V_O}$ is the DFT energy of the supercell with a V_O, $E_{\mathrm{DFT}}^{\mathrm{perf}}$ is the DFT energy of the perfect supercell with no defects, and μ_O is the chemical potential of oxygen in the system, calculated in the oxygen-rich limit as given in Eq. (3).

The formation energy of the V_O nearest neighbor (NN) to a dopant, with the dopant occupying the octahedral interstitial site of Al_2O_3) was calculated as

$$E_f = E_{\mathrm{DFT}}^{V_O-\mathrm{D}} - E_{\mathrm{DFT}}^{\mathrm{D}} + \mu_O, \quad (2)$$

where E_f is the formation energy of V_O at the NN site to the dopant, $E_{\mathrm{DFT}}^{V_O-\mathrm{D}}$ is the DFT energy of the supercell with the dopant and V_O at its NN site, $E_{\mathrm{DFT}}^{\mathrm{D}}$ is the DFT energy of the supercell with the dopant at the interstitial site, and μ_O is the chemical potential of oxygen in the system, calculated in the oxygen-rich limit at 300 K, i.e.,

$$\mu_O(T, P_{O_2}) = \frac{1}{2}\left[E_{O_2}^{\mathrm{DFT}} + E_{\mathrm{over}} + \mu_{O_2}^{0}(T, P^0) + kT\ln\left(\frac{P_{O_2}}{P^0}\right)\right], \quad (3)$$

where $E_{O_2}^{\mathrm{DFT}}$ is the DFT energy of the O_2 molecule; E_{over} is the correction for the O_2 overbinding error caused by GGA, taken as 1.36 eV, as identified by Wang *et al.* [56]; $\mu_{O_2}^{o}(T, P^o)$ is the difference in chemical potential of O_2 gas between $T = 0$ K and the temperature of interest (300 K), at a reference pressure of $P^0 = 1$ atm, as obtained from thermochemical tables; P_{O_2} is the partial pressure of oxygen gas (1 atm in the O-rich limit).

The cluster formation energy (per V_O) in undoped Al_2O_3 was calculated as

$$E_f = \frac{E_{\rm DFT}^{n{\rm V_O}} - E_{\rm DFT}^{\rm perf} + n\mu_{\rm O}}{n}, \quad (4)$$

and in doped Al_2O_3, it was calculated as

$$E_f = \frac{E_{\rm DFT}^{n{\rm V_O-D}} - E_{\rm DFT}^{\rm D} + n\mu_{\rm O}}{n}, \quad (5)$$

where E_f is the formation energy of V_O cluster in the undoped and doped case, respectively; $E_{\rm DFT}^{n{\rm V_O}}$ is the DFT energy of the supercell with only the $n{\rm V_O}$ ($n = 4$) cluster; $E_{\rm DFT}^{n{\rm V_O-D}}$ is the DFT energy of the supercell with the dopant and $n{\rm V_O}$ ($n = 4$) cluster; $E_{\rm DFT}^{\rm D}$ is the DFT energy of the supercell with only the dopant at the interstitial site; $E_{\rm DFT}^{\rm perf}$ is the DFT energy of the perfect supercell with no defects; and $\mu_{\rm O}$ is the chemical potential of oxygen in the system, calculated in the oxygen-rich limit as in Eq. (3).

The cluster binding energy (per V_O) in the undoped case was calculated as

$$E_b(n{\rm V_O}) = \frac{nE_f^{\rm V_O} - E_f^{n{\rm V_O}}}{n}, \quad (6)$$

and in the doped case, it was calculated as

$$E_b(n{\rm V_O\text{-}D}) = \frac{nE_f^{\rm V_O} + E_f^{\rm D} - E_f^{n{\rm V_O\text{-}D}}}{n}, \quad (7)$$

where $E_f^{\rm V_O}$, $E_f^{\rm D}$ have been defined before, and $E_f^{n{\rm V_O}}$, $E_f^{n{\rm V_O-D}}$ are the formation energies of the V_O cluster in the undoped and doped cases, respectively.

B. Experimental

1. Atomic layer deposition of WN/Al_2O_3 stack

Here, n-type degenerate Si wafers were purchased from University Wafer. Wafers were dipped in 1:50 HF:H_2O for 60 s to remove native oxide and spin rinsed dried. Next, a wafer was loaded into an Oxford FlexAL atomic layer deposition (ALD) machine for plasma-enhanced deposition of alternate layers of WN and Al_2O_3 to give the stack Si/7.5 nm WN/2.0 nm Al_2O_3/3.0 nm WN/2.0 nm Al_2O_3/3.0 nm WN/2.0 nm Al_2O_3. The bottom electrode of the resistive switching device is the 7.5 nm WN. The purpose of this WN is to build the stack starting from a well-defined layer to avoid wafer-to-wafer variations from an uncertified supply of Si wafers. WN is used instead of other commonly used metals due to complementary metal-oxide-semiconductor requirements imposed on this shared ALD machine. For a two- or one-layer Al_2O_3 device, the thickness of each oxide layer will be increased to 3.0 and 6.0 nm, respectively, so that the combined oxide layer thickness remains constant. Deposition was done at 300 °C. The deposition of WN is a N_2/H_2 plasma-enhanced reaction with bis(tert-butylimino)bis(dimethylamino)tungsten(VI) precursor. The deposition of Al_2O_3 is an O_2 plasma-enhanced reaction with trimethylaluminum precursor. Both recipes were supplied by the manufacturer. The thin film thicknesses were determined via x-ray reflectivity using a Rigaku SmartLab x-ray diffractometer, with both single films on wafers or composite films on wafers measured. The growth rates of WN and Al_2O_3 were deduced to be 0.5 and 1.0 Å/cy, respectively, on the Oxford FlexAL ALD machine.

2. Au deposition and FIB milling

Au deposition is typically performed on a Balzers tabletop sputterer at 130 V and 40 mA for 150 s to give a film thickness of 30 nm. There is no difference in device performance when Au is being deposited with a AJA International magnetron sputterer or an e-beam deposition machine. No additional metal adhesion layer is used for Au deposition. A 30 keV Ga ion beam on a FEI Helios NanoLab 600i DualBeam FIB/scanning electron microscope (SEM) was used to mill away material to produce a square mesa where each side of this square is 50 μm and the width of the milled border is 1 μm. The SEM mode was used to image the chip to setup for the FIB so there is no unintended FIB damage except as intended around the perimeter of the mesa. The milling was performed to a depth that exposes the Si substrate. This corresponds to an areal Ga ion dose of 80 to 120 $\rm pC/\mu m^2$. Resistive switching devices start in the low-resistance state (LRS) after ion beam milling without a need for electroforming.

3. Electrical measurements

Probing of the mesa was done with a 25-μm-diameter gold wire tip to contact the topmost Au film of a typical device on a custom-built probe station. The gold wire is soft and is great for avoiding scratches to the top film. Electrical contact to the bottom WN electrode was made through the degenerately doped Si substrate. A standard tungsten probe from Signatone (probe tip No. SE-T) can also be used. No difference in device performance was observed regardless of whether the probe is an Au wire or a tungsten probe. The stiffer tungsten probe was necessary if the top film was Cu, Al, or Ti and not Pt, Pd, or Au because the Au wire is unable to punch through the native oxide of these metals. A Keithley 2450 sourcemeter was used to source voltage and measure current.

III. RESULTS AND DISCUSSION

A. Effect of Au doping on device switching variability

We tested our hypothesis about the effect of dopant electronegativity on switching variability first on Au-doped Al_2O_3. Au is one of the most electronegative metals in the periodic table [57]. More than 100 samples of multilayer RRAM devices were fabricated and tested. These RRAM devices were made of alternating layers of Al_2O_3 separated by conductive WN layers, with Au as the top electrode and WN as the bottom electrode. The cross-section of the fabricated device, imaged using a transmission electron microscope (TEM), is shown in Fig. 1(a). The device schematic and the effect of Au doping on switching variability is shown in Figs. 1(b)–1(f). In Fig. 1(c), when FIB milling is used to define the device area after depositing the Au top electrode, the switching variability reduces dramatically. Estimations from Stopping and Range of Ions in Matter (SRIM) simulations indicate that the high-energy FIB milling process results in the implantation of Au atoms from the top electrode into the

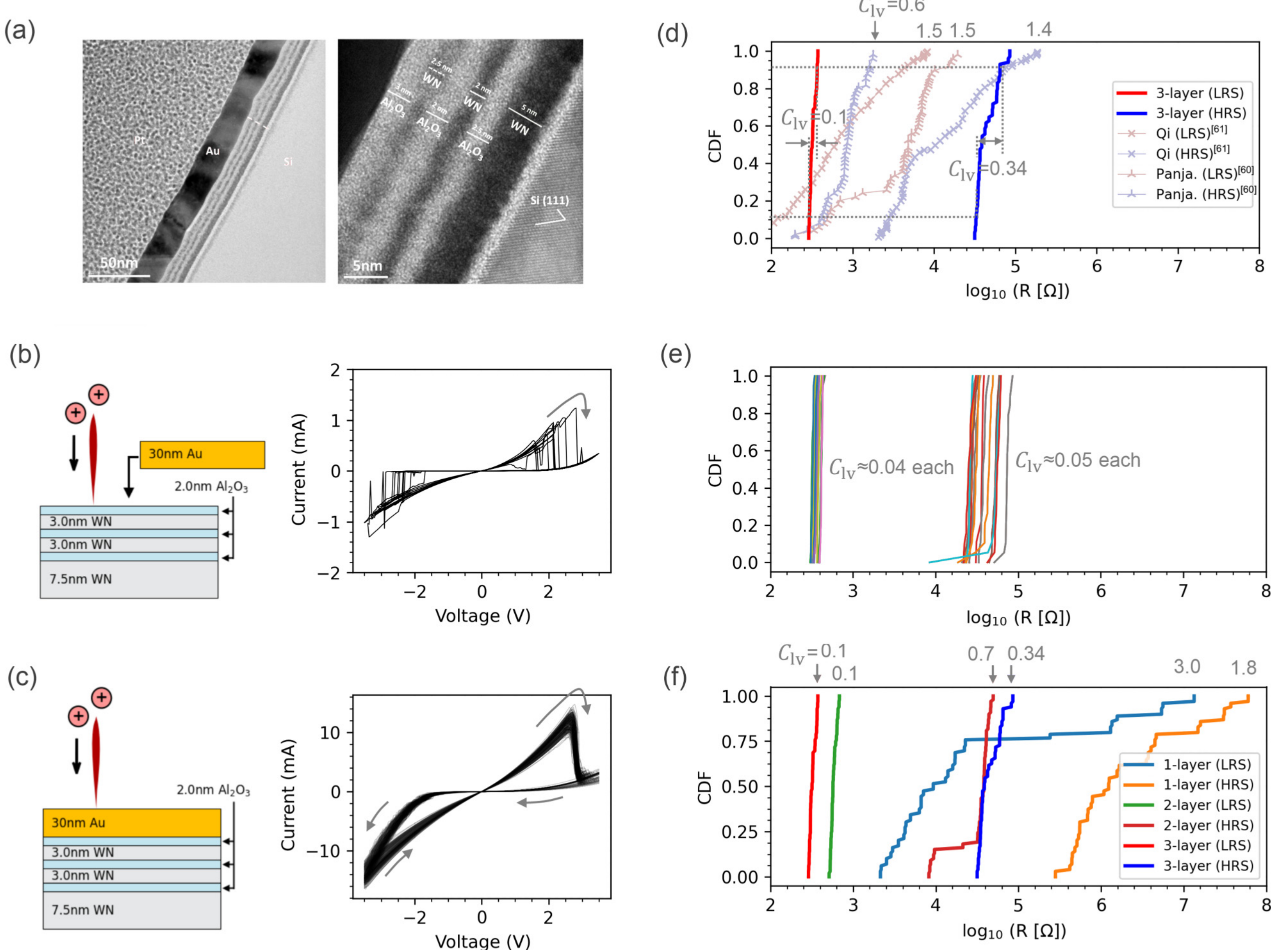

FIG. 1. Electronegative Au dopants and multilayering of the oxide films are two key factors to enable low variability switching. (a) Device cross-section imaged using transmission electron microscopy (TEM). For further elaboration on device design and TEM imaging, see Fig. 2 and Supplemental Material Fig. S7 [58]. Panels (b) and (c) compare the device performance without and with Au dopant implanted into the multilayered switching devices. (b) Multilayer Al_2O_3 cannot switch consistently when focused ion beam (FIB) milling is performed to define the device area before Au deposition. (c) Multilayer Al_2O_3 switches consistently when FIB milling is performed to define the device area after Au deposition. These devices did not require electroforming. The *I-V* plot shows 300 superimposed switching cycles (15 devices $\times 20$ consecutive cycles in each device). (d) The variability improvement using the Au doping strategy can be seen from the short span of resistances in the cumulative distribution functions (CDFs) observed over the 300 switching cycles, covering only 0.10 and 0.34 decades for the low-resistance state (LRS) and high-resistance state (HRS), respectively. Typical spans of other Al_2O_3 [60,61] devices from the literature are shown for comparison. (e) The device-to-device CDF in (d) can be displayed separately for the 15 devices to show cycle-to-cycle variations <0.05, indicating that most of the variation seen in (d) comes from device-to-device differences. (f) CDF plots show the narrowing of the spread in the LRS and HRS resistances from a few orders of magnitude down to 0.10 and 0.34, respectively, with increasing the number of oxide layers from one to three.

Al_2O_3 electrolyte (Supplemental Material Figs. S1–S3 [58]). This is a critical requirement for achieving superior switching characteristics because depositing the Au top electrode after FIB milling results in poor switching, as shown in Fig. 1(b). This rules out other hypotheses, such as implanted Ga and FIB milling damage, for the observed superior switching. Figures 1(d) and 1(e) show the cumulative distribution function (CDF) plots of the obtained high-resistance state (HRS) and LRS at the device level and at the cycle level, respectively. To evaluate the variability in LRS and HRS, we use an alternative and more reliable measure of switching variability, the logarithmic coefficient of variation (C_{lv}) [59], defined as the difference between the 10th and 90th percentile of the logarithm of resistance values. Compared with $C_{lv} \sim 1.5$ for other Al_2O_3-based RRAMs reported in the literature [60,61], our devices have significantly lower C_{lv} of 0.1 and 0.34 for the LRS and HRS, respectively, as plotted in Fig. 1(d). This slight switching variability arises mainly from fabrication-related variation, which may be further reduced by enforcing stringent manufacturing procedures. From Fig. 1(e), cycle-to-cycle variation has an even smaller spread of $\sim$0.04 and 0.05 for the LRS and HRS states, respectively. Thus, the intrinsic switching variability of each device is very low, indicating substantial reduction in the stochasticity of formation and rupture of conduction channels. Such low variability is valuable for facilitating multibit switching schemes [18] and meets and surpasses the reproducibility requirement (with a C_{lv} of $\sim$0.32) needed to implement accurate hardware neural

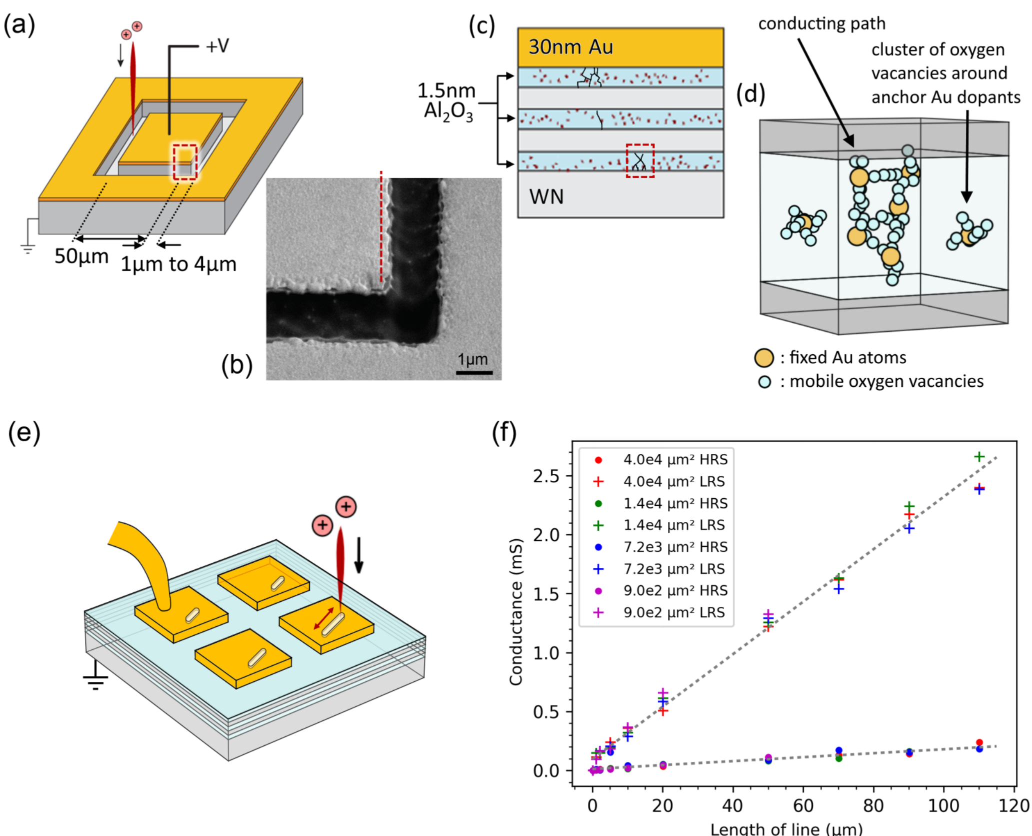

FIG. 2. Experimental investigation on the effect of focused ion beam (FIB)-processed device perimeter to measure conductance of individual devices at high-resistance state (HRS) and low-resistance state (LRS). (a) Three-dimensional (3D) perspective view of the FIB milling carried out to define the area of a single resistive switching device. (b) Scanning electron microscopy (SEM) image of region outlined with red dashed lines in (a). The darker region shows the exposed Si substrate, while the lighter regions are the top Au film. The red dash line [cross-section shown in (c)] will be affected by Au implantation due to the proximity to the FIB milling. (c) Stack schematic showing the layers deposited above a Si substrate. The FIB milling implants Au atoms sideways into the edge of Al_2O_3 layers. An atomistic schematic of the regions outlined in red dashed lines is shown in (d). (e) An alternative fabrication scheme where a 30-nm-thick Au contact pad of variable size was deposited with e-beam deposition through a shadowmask onto the usual triply repeated WN/Al_2O_3 stack. A line with variable length was then FIB milled into this Au contact pad. (f) Measured device conductance data indicates a linear relation with increasing FIB milled lengths but no dependence on the contact pad area.

networks [25]. Additionally, these multilayer, Au-implanted devices exhibit a perfect yield. All 100 devices under test are in LRS upon fabrication without the need for electroforming (shown in Supplemental Material Fig. S5 [58]). The complexity of peripheral circuitry in RRAM arrays is reduced without the functional need for electroforming, and the resulting higher yield from electroforming-free devices would lead to improved accuracy of neural networks [26]. Moreover, the devices exhibit resistive switching with a gradual SET transition. This gradual SET transition is key to multibit switching and analog processing, as explained in forthcoming sections.

Switching from HRS to LRS in our device is likely due to the formation of a network of cohesive clusters made of oxygen vacancies (V_O). The dependence of switching current on the FIB-processed device perimeter indicates areal switching, as shown in Fig. 2. Figure 2(a) shows the device schematic and denotes the dimensions of the device (50×50 µm) and the FIB milling region (1–4 µm width around the device). Figure 2(b) shows the SEM image of the device edge near the FIB-milled region. Figures 2(c) and 2(d), respectively, show the schematics of the multilayer device and the network of oxygen vacancies that likely form near the edges of the device (where Au is believed to be implanted). Figures 2(e) and 2(f) show the variation in device conductance with FIB milling length, where it is seen that increasing the length of the line increases the device conductance. Notably, there is no dependence of conductance on contact pad area. Thus, areal switching from Fig. 2(f) indicates the presence of a network of conducting zones near the periphery of the device. This conducting zone is potentially in the form of a network of conducting filaments; or in the limit of a dense network, it is made of a host chemistry with higher conductance. It is unlikely that conducting zone is made of Au filaments via dissolution of the Au top electrode. Au is resistant to oxidation and is in fact commonly used as the inert electrode in RRAM devices, as opposed to metals like Ag and Cu, which are typical active electrode candidates [62,63]. Additionally, the TEM image shown in Fig. 1(a) was taken at the edge of the device, where Au atoms are expected to be implanted (as per our SRIM calculations in Supplemental Material Fig. S3 [58]). If there indeed were metallic filaments of Au, they would have shown up as contrasts in the TEM image. Thus, we

believe that the role of the Au dopant is through its catalytic effect on V_O formation in Al_2O_3 rather than through Au metal filament formation. Future work can incorporate techniques like atom probe tomography to directly image the Au atoms, which is not possible to achieve with the detection limits of TEM and other spectroscopy techniques like electron energy loss spectroscopy and energy dispersive x-ray spectroscopy. Note also that, while Fig. 2(f) shows a linear scaling of the device conductance down to a FIB-milled length of 0.5 μm, switching of devices with nanometer dimensions might have more device-to-device variation due to the discrete atomistic nature of doping.

Low switching variability is observed in only multilayer devices doped with Au. The CDF plot for one-, two-, and three-layer devices in Fig. 1(f) shows that the switching variability improves as the number of layers is increased from one to three, while keeping the total thickness of Al_2O_3 constant. This is likely because thinner oxide layers require shorter conducting paths, thereby lowering stochasticity in the formation and disruption of conductive channels of oxygen vacancies bridged by Au dopants, giving rise to high uniformity as observed in previous studies on multilayer oxides [27–29,32]. Thus, having a multilayer and Au-doped electrolyte together form a necessary and sufficient condition to achieve low switching variability in our system.

B. Effect of Au doping on switching variability: Model based on first-principles calculations

We have carried out DFT calculations to identify the effect of Au doping on neutral oxygen vacancy (V_O) formation. Irradiation processes such as FIB milling result in the creation and distribution of defects such as vacancies and interstitials. Here, we focus on the effect of Au at the interstitial site in Al_2O_3. The concentration of dopants in our simulations is ∼4%. This is consistent with the range of implanted dopant concentration as estimated by SRIM simulations (shown in Supplemental Material Fig. S3 [58]). Table I shows the formation energy of V_O in undoped Al_2O_3 and at the NN site of the interstitial Au dopant in Al_2O_3. The formation energy of V_O next to the Au dopant is drastically lowered by >6 eV. This indicates that V_O preferentially forms at the vicinity of the Au interstitial dopant. Since the Au atoms are pinned and stationary, the locations at which V_O is formed are also fixed. This minimizes the randomness in V_O formation, thus creating defined local regions that are easily reduced, which then connect to form conducting paths.

In addition to the ease of formation of V_O point defects, it is important to investigate the effect of the Au dopant on V_O cluster formation. V_O clusters act as building blocks for the formation of conducting paths or networks of conducting channels via which resistive switching occurs. Table I shows the calculated V_O cluster formation energies in undoped and Au-doped Al_2O_3. Cluster formation energy (per V_O) represents the tendency of forming a V_O cluster in the presence of Au. Introduction of the Au dopant into the cluster markedly lowers cluster formation energy.

The reduction in the formation energy of V_O next to the Au dopant can be rationalized by investigating the density of states (DOS) and electron redistribution of the

TABLE I. (left) V_O formation energies in undoped Al_2O_3 and at the NN site of the interstitial dopants (Au, Pt, Pd, Cu, Ti, and excess Al) in doped Al_2O_3. (right) V_O cluster formation energies and binding energies (per V_O) in undoped and doped Al_2O_3.

Defect	Formation energy (eV)	Binding energy (eV)
V_O	7.19	
V_O NN to Au	0.64	
V_O NN to Pt	0.47	
V_O NN to Pd	1.91	
V_O NN to Cu	3.61	
V_O NN to Ti	4.38	
V_O NN to Al	3.63	
Defect cluster type		
V_O cluster	7.01	0.18
V_O cluster with Au	4.32	2.87
V_O cluster with Pt	4.73	2.48
V_O cluster with Pd	4.73	2.48
V_O cluster with Cu	5.29	1.90
V_O cluster with Ti	5.36	1.83
V_O cluster with Al	5.40	1.79

doped Al_2O_3 system. Oxygen vacancy formation in undoped Al_2O_3 is an energetically costly process because the electrons that are left behind upon removing an oxygen atom cannot occupy the high energy, empty cation states and, consequently, localize at the oxygen vacancy site. In contrast, in the DOS plots of the Au-doped Al_2O_3 shown in Figs. 3(a)(i) and 3(a)(ii), the Au interstitial introduces additional states at the valence band maximum (VBM) of Al_2O_3 along with midgap states. Upon the removal of an oxygen atom, the low-lying midgap states trap the electrons left behind, completing the Au 6*s* orbital electron configuration ($[Xe]4f^{14}5d^{10}6s^1 \rightarrow [\mathrm{Xe}]4f^{14}5d^{10}6s^2$). The ability to uptake these electrons to the low-energy states decreases the V_O formation energy. This capture mechanism of electrons from V_O by the Au atom can be seen in the DOS plot in Fig. 3(a)(ii), where the Au midgap states shift lower in energy. The corresponding partial charge density plot of the midgap states is shown in Fig. 3(b), where an electron cloud around Au is clearly seen.

Additionally, Au is a noble metal with a high electronegativity of 2.3 [57], close to that of oxygen. This leads to electron redistribution from Al to Au in Al_2O_3, facilitated by Au electronic states near the VBM of Al_2O_3, as noted above and shown in Figs. 3(a)(i) and 3(a)(ii). The calculated Bader charges [64,65] (relative to the respective neutral atom) on Au, NN Al, and NN O in Au-doped Al_2O_3 are −0.4 e, +2.41 e, and −1.55 e, respectively. The magnitude of charge on NN O is lower than in the undoped case, where O has a charge of −1.65 e. The presence of the Au dopant thus leads to electron transfer from Al to the Au atom instead of to O. Charge transfer from Al to Au weakens the NN Al-O bonds in the Al_2O_3 lattice, resulting in the lowering of the V_O formation energy. Electron transfer from Al_2O_3 to the Au dopant has been observed experimentally in prior work [66,67], for example, in Au-Al_2O_3 nanocomposites [67] as well as upon adsorption of Au monomers on Al_2O_3/NiAl [66].

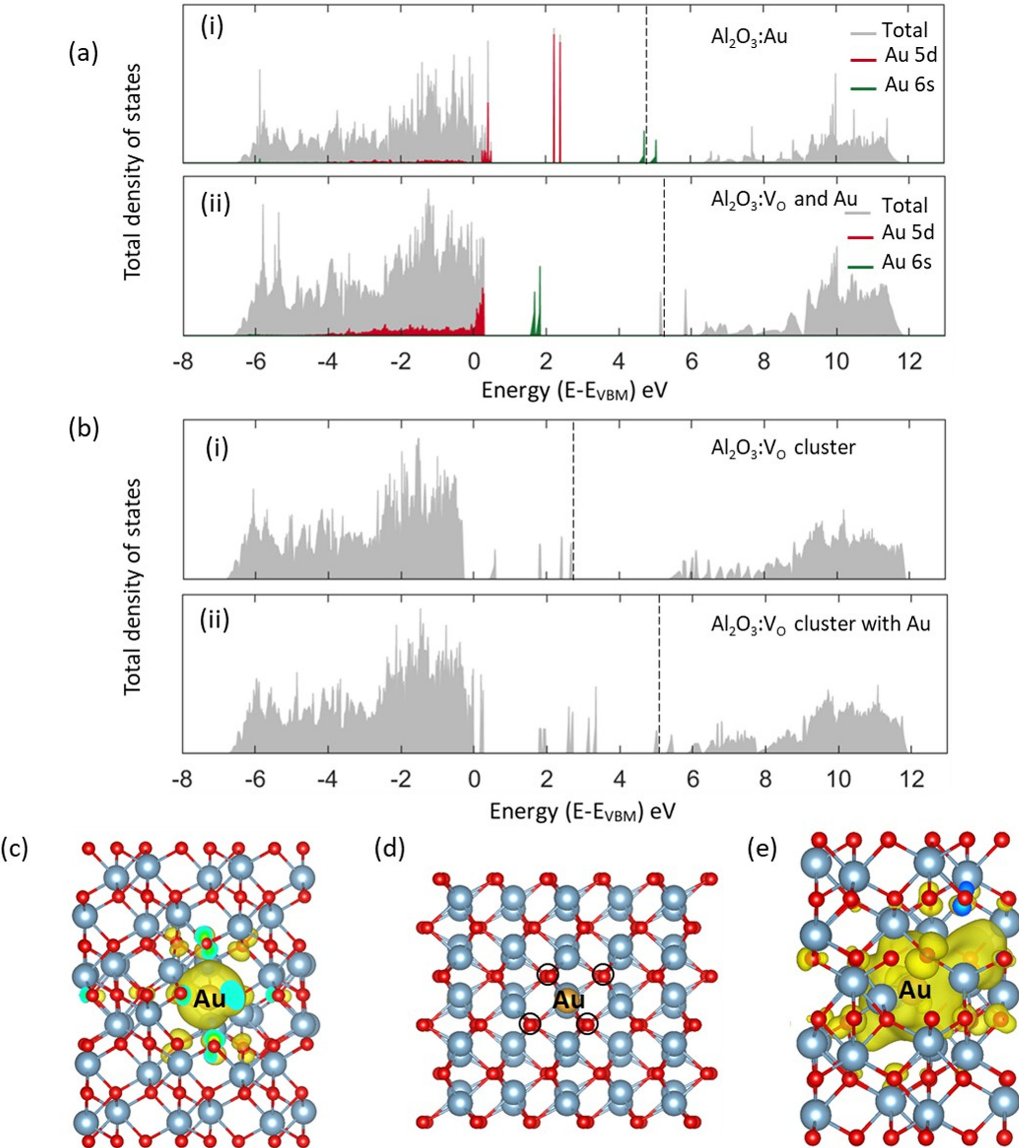

FIG. 3. (a) Total density of states (DOS) of (i) Au-doped Al_2O_3 and (ii) Au-doped Al_2O_3 with one V_O at nearest neighbor (NN) site to Au. (b) Total DOS of (i) undoped Al_2O_3 with a 4-V_O cluster and (ii) Au-doped Al_2O_3 with a 4-V_O cluster. In all DOS plots, the valance band maximum is at 0 eV, and both spin-up and spin-down states are plotted. The dotted line marks the position of the Fermi level. (c) Band decomposed charge density profile of Au s orbital in relaxed Au-doped Al_2O_3 with a single V_O (isosurface: $0.003\,\mathrm{eV/Å^3}$), showing charge transfer to Au. (d) Initial structure of the V_O cluster in Au-doped Al_2O_3 (positions of the NN V_O are marked by black circles). (e) Band decomposed charge density profile of electronic states within the bandgap for the relaxed Au-doped Al_2O_3 with a 4-V_O cluster around Au (isosurface: $0.01\,\mathrm{eV/Å^3}$).

The initial structure of the Au-doped V_O cluster with Au at the interstitial site in Al_2O_3 is shown in Fig. 3(d), with the positions of V_O marked with black circles. The oxygen vacancy cluster introduces multiple discrete midgap states, shown in Figs. 3(b)(i) and 3(b)(ii). Introducing Au gives rise to additional midgap states, particularly near the top of the valence band and the bottom of the conduction band. As seen in Fig. 3(b), the dominant midgap states are from V_O, and these states can provide a path for electrons to tunnel through the oxide barrier from the cathode to the anode [16]. It is expected that, as the concentration of oxygen vacancies increases under applied field, the number of localized states from V_O in the bandgap will increase, ultimately closing the bandgap, giving rise to metallic conduction. In fact, this is seen in the DOS plots of the Au-doped vacancy filament path model in Supplemental Material Figs. S9 and S10 (additional details regarding the filament model can be found in Tables S1–S3) [58]. The partial charge density of all the defect states within the bandgap of the relaxed, Au-doped system with a V_O cluster is shown in Fig. 3(e), revealing a localized, conductive cluster arising from the states introduced by oxygen vacancies.

Next, we assess the V_O cluster binding energies which are reflective of the preferential position of vacancy or vacancy cluster formation. Table I tabulates the V_O cluster binding energies in undoped and Au-doped Al_2O_3. Cluster

binding energy (per V_O), calculated as $E_b(nV_O{-}D) = (nE_f^{V_O} + E_f^D - E_f^{nV_O-D})/n$, represents the energy required to dissociate the cluster into isolated V_O and Au. The binding energy of the V_O cluster in the undoped case as calculated in this paper matches well with previous theoretical studies on V_O chains [68] and V_O pairs [69]. The presence of the Au dopant increases cluster binding energy (per V_O). The positive binding energy indicates that the cluster is cohesive. Thus, introduction of Au not only makes V_O cluster formation more energetically favorable but also enhances cluster cohesion. Such short-range cohesive clusters can then act as building blocks for the formation of conducting paths across the entire oxide layer. When Au is present, formation of vacancies and vacancy clusters preferentially occur near the Au atoms, thereby reducing stochasticity in the formation of conducting paths and increasing the cohesion and stability of these paths.

Given the favorable formation and binding energies of V_O and V_O clusters near the Au dopant, a reasonable question arises about whether this binding leads to a reduction in mobility of V_O. As shown in Supplemental Material Figs. S11–S13 and Tables S4 and S5 [58], we have calculated V_O migration barriers in the Au-doped system. In all the paths studied, we find that the migration barriers are lower by ~0.5 eV compared with that in undoped Al_2O_3. Thus, V_O is more mobile in the Au-doped system than the undoped system. This is due to charge transfer from V_O to Au, reducing the trapped electron density in V_O, and thereby making the migration of V_O easier than in the undoped Al_2O_3. These results reveal favorable implications for switching speed and energetics via V_O formation and migration in Au-doped Al_2O_3.

It is worthwhile to add here that, in this paper, we focus only on neutral defects, such as neutral oxygen vacancies. This is because the conductive networks in Al_2O_3 arise from cohesion between these neutral defects, making them the most important defect to consider [68]. However, it is important to note that high-energy irradiation processes such as FIB milling can create a wide range of defects with nonequilibrium concentrations and different charge states. A thorough investigation of these defects would require other methods such as Monte Carlo or molecular dynamics approaches, which is out of scope for this paper but is of key interest for future studies. Finally, we also clarify here that the trends in binding energy given in Table I will hold irrespective of the Fermi level or the chemical potential of the species since complex formation does not change the number and nature of participating species.

C. Prediction of other dopants and their device tests

Given the above proposed connection between dopant electronegativity and switching variability as explained in the previous section, we have assessed the effect of more and less electronegative dopants on the V_O point defect and Vo cluster formation energies and on device switching repeatability. A range of dopants across the electronegativity scale [57] was studied, namely, Pt (2.1), Pd (2.0), Cu (1.8), Ti (1.6), and Al (1.5) interstitials. This expands the device design space as well as further strengthens the link between dopant electronegativity and device variability.

As seen in Table I, while the formation energy of NN V_O is generally lowered regardless of the interstitial dopant, for the highly electronegative Pt and Pd dopants, the formation energy is very significantly lowered. Thus, like Au, electronegative dopants like Pt and Pd also reduce the V_O point defect and cluster formation energy considerably and have higher cluster binding energy. The relaxed structures of V_O at the NN site of these interstitial dopants can be found in Supplemental Material Fig. S14 [58], and the total DOS of the doped V_O clusters can be seen in Supplemental Material Fig. S15 [58].

Bader charge analysis [64,65] revealed that, like the case with Au, charge transfer takes place from Al to Pt and Pd but not to Cu, Ti, or Al interstitial (Supplemental Material Table S6 [58]). Investigating the electronic DOS, low-lying states near the VBM and midgap states are observed in the Pt- and Pd-doped cases as well but not in the Al-, Cu-, and Ti-doped cases (see Supplemental Material Fig. S16 [58] for local DOS plots for all cases). The states near the VBM facilitate electron redistribution around the electronegative Pt and Pd dopants, easing Al-O bond breakage. The midgap states trap the electrons left behind upon removal of an oxygen atom, thus lowering V_O formation energy significantly.

It is noteworthy to point out here that, while the difference between the electronegative and nonelectronegative elements is clear, the relative trend between the electronegative dopants can also be explained. Here, V_O defect formation energy next to Au and Pt is lower than Pd by $>\sim 1$ eV. This can be attributed to the relativistic contraction of the *s* and *p* orbitals of Au and Pt due to their significantly higher mass than Pd. As explained by Pyykko and Desclaux [70], this contraction leads to the 6*s* state of Pt and Au lying deeper in the atom (as compared with that in Pd [71]), resulting in significant energy gains upon filling it.

We have validated these predictions on the role of electronegativity of the dopant on creating preferential zones of higher conductivity by performing switching experiments on these compositions. Multilayer devices with the same geometry as shown in Fig. 1(c) were fabricated with Pt, Pd, Cu, Ti, and Al top electrode layers and FIB milled after top electrode deposition to define the device area. The *I-V* curves and corresponding CDF plots are shown in Fig. 4. In line with our computational predictions, devices doped with noble metals with high electronegativities such as Pt and Pd exhibit markedly consistent switching behaviors, whereas the more reactive metals with lower electronegativities are seen to have erratic switching cycles. It is highly encouraging that the consistent switching of the Au/Pt/Pd-doped devices is seen across multiple devices. We recognize that our top electrode/Al_2O_3 interface changes along with the implanted dopant, which could be an additional cause behind the different switching properties. However, previous studies have found that the top metal electrode has a limited effect on the switching properties [72]. Additionally, if our devices were dependent entirely only on the Schottky barrier changes at different metal/Al_2O_3 interfaces, we should have observed a dependence on the metal contact before the FIB milling was done. However, we see a dependence on the metal only after FIB milling. This indicates that the implanted dopants play the main role in ensuring low switching variability. However,

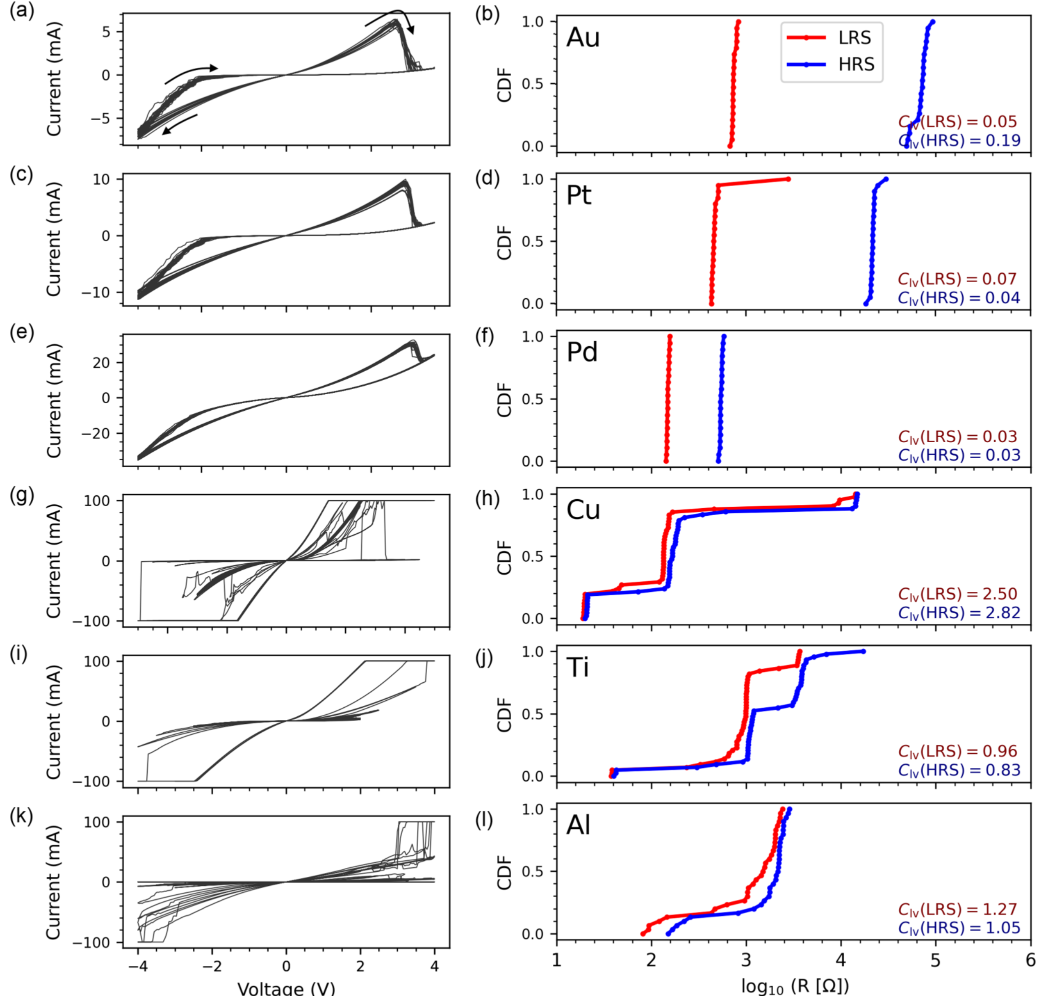

FIG. 4. Dopant metals from a range of electronegativities (a) Au, (c) Pt, (e) Pd, (g) Cu, (i) Ti, and (k) Al were tested to observe their effects on switching variability of Al_2O_3. Cumulative distribution functions (CDFs) for the low-resistance state (LRS) and high-resistance state (HRS) are plotted in (b), (d), (f), (h), (j), and (l). Dopants with higher electronegativities (Au, Pt, and Pd) have CDF plots with narrower widths, indicating that Al_2O_3 layers doped with these metals have low variability switching, consistent with predictions of easier V_O and V_O cluster formation shown in Table I and Fig. 3.

to unequivocally rule out the effect of the top electrode/Al_2O_3 interface, future studies could use commercial ion implanters to directly implant the different metal dopants while keeping the top electrode material the same across devices. We also recognize that there is room for improvement for increasing the resistances of the HRS of these devices. Since our devices switch via an areal mechanism, this can be achieved by scaling the device down laterally to limit the size of the conductive network that participates in the switching. Dopants with lower electronegativities (Cu, Ti, and Al) exhibit erratic switching, with poor ON-OFF ratios. Here, C_{lv} of the devices doped with the more electronegative metals is almost two orders of magnitude lower than those doped with Cu, Ti, and Al. Finally, we recognize that the dopants employed also differ based on their *n*- vs *p*-type nature. Further investigation of the observed trends based on *n*- and *p*-type nature of the dopants would be interesting. However, this would require evaluating the equilibrium Fermi level established upon doping Al_2O_3 and the resulting defect compensation mechanisms, which was not the focus of this paper. Additionally, given the high-energy irradiation process of FIB milling, it is unlikely that such equilibrium trends will be established in the material. Therefore, we focused on linking the dopant electronegativity on the V_O formation energies in this paper. However, we plan to account for the *p*- vs *n*-type nature of dopants in our future work.

D. Multibit switching

This high switching consistency demonstrated by Au, Pt, and Pd dopants in Al_2O_3 is beneficial for achieving multibit switching. From the *I*-*V* plots in Fig. 5 [and also in Figs. 4(a), 4(c), and 4(e)], it can be observed that these doped devices exhibit a gradual SET transition. The gradual SET transition allows the modulation of resistance states in a continuous manner, a key requirement for analog computing. The choice of a different terminating cycle voltage in the voltage-sweep measurements leads to different final resistance states with distinct *I*-*V* traces, as seen in Fig. 5(a). A more negative terminating voltage puts the device in a more conductive LRS

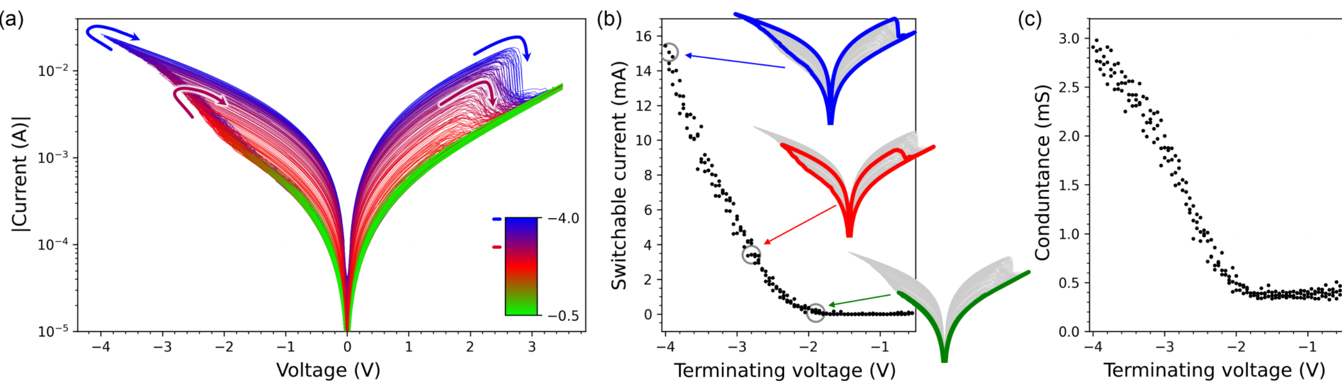

FIG. 5. The gradual SET process is convenient for demonstrating multibit switching in Al_2O_3. (a) Multiple switching cycles were performed with variable terminating voltages between −0.5 to −4 V and a fixed maximum voltage at 3.5 V. Each switching cycle is color coded according to the most negative terminating voltage used. For example, a voltage sweep from −4 to 3.5 V is shown in blue, has the largest hysteresis that indicates the largest extent of switching, and the sharpest RESET onset at ∼2.8 V. On the other hand, a voltage sweep from −1 to 3.5 V is shown in green and has barely any hysteresis or switching. The simple use of a chosen terminating voltage can put the device into a predictable state, as characterized by (b) the switchable current and (c) the device conductance. The switchable current is defined as the difference in the device current as set and the lowest current measured in the OFF (highest resistance) state. Green, red, and blue overlays in (b) show the nature of one *I-V* sweep when the device is set by −2, −2.8, and −3.9 V as terminating voltages, respectively. No current compliance was needed to be programmed in the sourcemeter used for these measurements.

state [plotted in Figs. 5(b) and 5(c)] and subsequently also has a RESET transition that occurs at a larger voltage. The gradual increase in conductivity during SET is likely via the increase in the volume and/or number of conductive pathways [16]. One possible mechanism for the controllable multibit switching is the lowered formation energy of oxygen vacancies, along with their distribution next to the electronegative dopants, that aid in the formation of multiple short conductive clusters with gradual increases in the magnitude of applied bias. The larger the change in the resistance state upon set, the larger the positive reset voltage that is needed, as also seen in Fig. 5(a). It is worthwhile to point out here that this multibit switching is demonstrated using a blind strategy, i.e., without any feedback control to read the resistance state and adjust. Additionally, no external control circuitry was used to enforce a SET current compliance. This simplifies the circuit design significantly, which will be useful in reducing the effective footprint of each cell for future multibit RRAM arrays. This feature of multilevel resistance states, along with the superior switching variability, makes these devices favorable candidates for multibit resistive switching. The multibit switching exhibited here could also extend the range of programming options for neuromorphic computing applications [73–75] which currently relies on voltage or current pulses to update each device.

IV. CONCLUSIONS

In conclusion, in this paper, we have identified that doping the insulating oxide electrolyte in the RRAM device with electronegative metal dopants can potentially improve the device switching variability. Our computational analysis reveals that electronegative dopants act as preferential sites for the formation of V_O point defects and clusters and increase the binding energy of the Vo clusters in Al_2O_3. This is because the midgap states introduced by the electronegative metal dopants capture the electrons left behind upon removal of oxygen and weaken Al-O bonds, facilitating V_O formation. These clusters then act as building blocks for the formation of conductive and cohesive V_O networks. Thus, electronegative dopants reduce the number of possible conductive pathways and thereby increase the uniformity of each device. Additionally, the midgap states that are introduced dominantly by the V_O clusters provide a path for easy electron conduction. The devices doped with electronegative dopants, Au, Pt, and Pd, have a cycle-to-cycle variation of just ∼0.05 in log-scale for the HRS and LRS and have a logarithmic coefficient of variation almost two orders of magnitude lower than those doped with active elements, Cu, Ti, and Al. This high uniformity, coupled with the gradual SET transition of the device, was used to demonstrate multibit switching capability without any external circuitry. Thus, the methods in this paper can enable the development of a high-yield, electroforming-free RRAM device, superior switching variability, and multibit capability. While there may be Schottky barrier changes at the top electrode/Al_2O_3 interface due to the different metal contacts, our findings indicate that the doping arising from FIB milling is likely the main effect behind low switching variability. To unequivocally resolve the two effects, future studies could use direct ion implantation techniques to implant the dopant atoms into the electrolyte, while keeping the top electrode/electrolyte interface fixed. Future experiments could also incorporate atom probe tomography to image the implanted dopant atoms. This will benefit efforts in RRAM device design and integration into crossbar arrays for use in neuromorphic computing applications [83].

ACKNOWLEDGMENTS

This paper made use of Microsystems Technology Laboratories at MIT for supporting fabrication. Shared Experimental Facilities, supported in part by the Materials Research Science and Engineering Centers Program of the National Science Foundation under Award No. DMR-1419807, supported FIB

work. The Institute for Soldier Nanotechnologies supported characterization. The DFT calculations were performed on the Cori system, which belongs to the National Energy Research Scientific Computing Center, a U.S. Department of Energy Office of Science User Facility located at Lawrence Berkeley National Laboratory, operated under Contract No. DE-AC02-05CH11231. Z.J.T. is grateful for scholarship funding from the Agency for Science, Technology and Research, Singapore.

[1] D. Ielmini and H.-S. P. Wong, Nat. Electron. **1**, 333 (2018).
[2] Y. Yang and W. Lu, Nanoscale **5**, 10076 (2013).
[3] X. Yao, K. Klyukin, W. Lu, M. Onen, S. Ryu, D. Kim, N. Emond, I. Waluyo, A. Hunt, and J. A. Del Alamo, Nat. Commun. **11**, 3134 (2020).
[4] N. K. Upadhyay, H. Jiang, Z. Wang, S. Asapu, Q. Xia, and J. Joshua Yang, Adv. Mater. Technol. **4**, 1800589 (2019).
[5] A. Chen, Solid State Electron. **125**, 25 (2016).
[6] S. Yu and P.-Y. Chen, IEEE Solid-State Circuits Mag. **8**, 43 (2016).
[7] E. Linn, R. Rosezin, C. Kügeler, and R. Waser, Nat. Mater. **9**, 403 (2010).
[8] T. Hasegawa, K. Terabe, T. Tsuruoka, and M. Aono, Adv. Mater. **24**, 252 (2012).
[9] Z. Wang, S. Joshi, S. E. Savel'ev, H. Jiang, R. Midya, P. Lin, M. Hu, N. Ge, J. P. Strachan, Z. Li *et al.*, Nat. Mater. **16**, 101 (2017).
[10] K. N. Subedi, K. Prasai, M. N. Kozicki, and D. A. Drabold, Phys. Rev. Mater. **3**, 065605 (2019).
[11] J. J. Yang, F. Miao, M. D. Pickett, D. A. Ohlberg, D. R. Stewart, C. N. Lau, and R. S. Williams, Nanotechnology **20**, 215201 (2009).
[12] R. Schmitt, J. Spring, R. Korobko, and J. L. Rupp, ACS nano **11**, 8881 (2017).
[13] D. Kuzum, R. G. D. Jeyasingh, B. Lee, and H. S. P. Wong, Nano Lett. **12**, 2179 (2012).
[14] J. Tang, F. Yuan, X. Shen, Z. Wang, M. Rao, Y. He, Y. Sun, X. Li, W. Zhang, and Y. Li, Adv. Mater. **31**, 1902761 (2019).
[15] G. Molas, G. Sassine, C. Nail, D. A. Robayo, J.-F. Nodin, C. Cagli, J. Coignus, P. Blaise, and E. Nowak, ECS Trans. **86**, 35 (2018).
[16] H.-S. P. Wong, H.-Y. Lee, S. Yu, Y.-S. Chen, Y. Wu, P.-S. Chen, B. Lee, F. T. Chen, and M.-J. Tsai, Proc. IEEE **100**, 1951 (2012).
[17] D. Kuzum, S. Yu, and H. P. Wong, Nanotechnology **24**, 382001 (2013).
[18] M. Lanza, H. S. P. Wong, E. Pop, D. Ielmini, D. Strukov, B. C. Regan, L. Larcher, M. A. Villena, J. J. Yang, and L. Goux, Adv. Electron. Mater. **5**, 1800143 (2019).
[19] A. Mehonic, A. L. Shluger, D. Gao, I. Valov, E. Miranda, D. Ielmini, A. Bricalli, E. Ambrosi, C. Li, and J. J. Yang, Adv. Mater. **30**, 1801187 (2018).
[20] Y. Wang, Q. Liu, H. Lü, S. Long, W. Wang, Y. Li, S. Zhang, W. Lian, J. Yang, and M. Liu, Chin. Sci. Bull. **57**, 1235 (2012).
[21] Y. M. Lu, M. Noman, W. Chen, P. A. Salvador, J. A. Bain, and M. Skowronski, J. Phys. D: Appl. Phys. **45**, 395101 (2012).
[22] D. Veksler, G. Bersuker, A. W. Bushmaker, P. R. Shrestha, K. P. Cheung, and J. P. Campbell, in *Proceedings of the 2019 IEEE International Reliability Physics Symposium (IRPS)* (IEEE, New York, 2019), pp. 1–5.
[23] C. Baeumer, R. Valenta, C. Schmitz, A. Locatelli, T. O. Mentes, S. P. Rogers, A. Sala, N. Raab, S. Nemsak, and M. Shim, ACS Nano **11**, 6921 (2017).
[24] D. S. Jeong, R. Thomas, R. Katiyar, J. Scott, H. Kohlstedt, A. Petraru, and C. S. Hwang, Rep. Prog. Phys. **75**, 076502 (2012).
[25] T. Gokmen and Y. Vlasov, Front. Neurosci. **10**, 333 (2016).
[26] C. Li, D. Belkin, Y. Li, P. Yan, M. Hu, N. Ge, H. Jiang, E. Montgomery, P. Lin, Z. Wang *et al.*, Nat. Commun. **9**, 2385 (2018).
[27] M. Akbari, M.-K. Kim, D. Kim, and J.-S. Lee, RSC Adv. **7**, 16704 (2017).
[28] J. Woo, K. Moon, J. Song, S. Lee, M. Kwak, J. Park, and H. Hwang, IEEE Electron Device Lett. **37**, 994 (2016).
[29] W. Banerjee, X. Xu, H. Lv, Q. Liu, S. Long, and M. Liu, ACS Omega **2**, 6888 (2017).
[30] T.-H. Kim, H. Nili, M.-H. Kim, K. K. Min, B.-G. Park, and H. Kim, Appl. Phys. Lett. **117**, 152103 (2020).
[31] S. Kim, T.-H. Kim, H. Kim, and B.-G. Park, Appl. Phys. Lett. **117**, 202106 (2020).
[32] Z. Fang, H. Yu, X. Li, N. Singh, G. Lo, and D. Kwong, IEEE Electron Device Lett. **32**, 566 (2011).
[33] A. Zalar, J. Van Lier, E. Mittemeijer, and J. Kovač, Surf. Interface Anal. **34**, 514 (2002).
[34] L. Chen, H.-Y. Gou, Q.-Q. Sun, P. Zhou, H.-L. Lu, P.-F. Wang, S.-J. Ding, and D. Zhang, IEEE Electron Device Lett. **32**, 794 (2011).
[35] L. Gao, Y. Li, Q. Li, Z. Song, and F. Ma, Nanotechnology **28**, 215201 (2017).
[36] J. H. Yoon, J. H. Han, J. S. Jung, W. Jeon, G. H. Kim, S. J. Song, J. Y. Seok, K. J. Yoon, M. H. Lee, and C. S. Hwang, Adv. Mater. **25**, 1987 (2013).
[37] S. Kim, S. Choi, J. Lee, and W. D. Lu, ACS Nano **8**, 10262 (2014).
[38] C.-S. Peng, W.-Y. Chang, Y.-H. Lee, M.-H. Lin, F. Chen, and M.-J. Tsai, Electrochem. Solid State Lett. **15**, H88 (2012).
[39] Z. Wang, W. Zhu, A. Du, L. Wu, Z. Fang, X. A. Tran, W. Liu, K. Zhang, and H.-Y. Yu, IEEE Trans. Electron Devices **59**, 1203 (2012).
[40] B. Gao, H. W. Zhang, S. Yu, B. Sun, L. F. Liu, X. Y. Liu, Y. Wang, R. Q. Han, J. F. Kang, B. Yu *et al.*, in *Proceedings of the 2009 Symposium on VLSI Technology* (IEEE, New York, 2009), pp. 30–31.
[41] Q. Liu, W. Guan, S. Long, M. Liu, S. Zhang, Q. Wang, and J. Chen, J. Appl. Phys. **104**, 114514 (2008).
[42] T. Tan, T. Guo, and Z. Liu, J. Alloys Compd. **610**, 388 (2014).
[43] H. Zhang, B. Gao, B. Sun, G. Chen, L. Zeng, L. Liu, X. Liu, J. Lu, R. Han, and J. Kang, Appl. Phys. Lett. **96**, 123502 (2010).
[44] S. Roy, G. Niu, Q. Wang, Y. Wang, Y. Zhang, H. Wu, S. Zhai, P. Shi, S. Song, and Z. Song, ACS Appl. Mater. Interfaces **12**, 10648 (2020).

[45] T. Kempen, R. Waser, and V. Rana, in *Proceedings of the 2021 IEEE International Memory Workshop (IMW)* (IEEE, New York, 2021), pp. 1–4.
[46] X. Xiang, Z. He, J. Rao, Z. Fan, X. Wang, and Y. Chen, ACS Appl. Electron. Mater. **3**, 1031 (2021).
[47] H. Jiang and D. A. Stewart, ACS Appl. Mater. Interfaces **9**, 16296 (2017).
[48] M. Y. Yang, K. Kamiya, H. Shirakawa, B. Magyari-Köpe, Y. Nishi, and K. Shiraishi, Appl. Phys. Express **7**, 074202 (2014).
[49] L. Zhao, S.-G. Park, B. Magyari-Köpe, and Y. Nishi, Appl. Phys. Lett. **102**, 083506 (2013).
[50] X.-D. Huang, Y. Li, H.-Y. Li, K.-H. Xue, X. Wang, and X.-S. Miao, IEEE Electron Device Lett. **41**, 549 (2020).
[51] V. Shapovalov and H. Metiu, J. Catal. **245**, 205 (2007).
[52] J. S. Becker, S. Suh, S. Wang, and R. G. Gordon, Chem. Mater. **15**, 2969 (2003).
[53] G. Kresse and D. Joubert, Phys. Rev. B **59**, 1758 (1999).
[54] J. P. Perdew, K. Burke, and M. Ernzerhof, Phys. Rev. Lett. **77**, 3865 (1996).
[55] G. Kresse and J. Furthmüller, Comput. Mater. Sci. **6**, 15 (1996).
[56] L. Wang, T. Maxisch, and G. Ceder, Phys. Rev. B **73**, 195107 (2006).
[57] W. Gordy and W. O. Thomas, J. Chem. Phys. **24**, 439 (1956).
[58] See Supplemental Material at http://link.aps.org/supplemental/10.1103/PhysRevMaterials.6.105002 for additional experimental and simulation details, materials, and methods which includes Refs. [76–83].
[59] Z. J. Tan and N. X. Fang, IEEE Electron Device Lett. **40**, 1546 (2019).
[60] R. Panja, S. Roy, D. Jana, and S. Maikap, Nanoscale Res. Lett. **9**, 692 (2014).
[61] Y. Qi, C. Z. Zhao, C. Liu, Y. Fang, J. He, T. Luo, L. Yang, and C. Zhao, Semicond. Sci. Technol. **33**, 045003 (2018).
[62] D. Jana, S. Roy, R. Panja, M. Dutta, S. Z. Rahaman, R. Mahapatra, and S. Maikap, Nanoscale Res. Lett. **10**, 188 (2015).
[63] R. Waser, R. Dittmann, G. Staikov, and K. Szot, Adv. Mater. **21**, 2632 (2009).
[64] R. F. Bader, Chem. Rev. **91**, 893 (1991).
[65] W. Tang, E. Sanville, and G. Henkelman, J. Phys.: Condens. Matter **21**, 084204 (2009).
[66] N. Nilius, M. V. Ganduglia-Pirovano, V. Brázdová, M. Kulawik, J. Sauer, and H.-J. Freund, Phys. Rev. Lett. **100**, 096802 (2008).
[67] J. Garcıa-Serrano, A. Galindo, and U. Pal, Sol. Energy Mater. Sol. Cells **82**, 291 (2004).
[68] M. Y. Yang, K. Kamiya, B. Magyari-Köpe, H. Momida, T. Ohno, M. Niwa, Y. Nishi, and K. Shiraishi, Jpn. J. Appl. Phys. **52**, 04CD11 (2013).
[69] J. A. Dawson and J. Robertson, J. Phys. Chem. C **120**, 14474 (2016).
[70] P. Pyykko and J. P. Desclaux, Acc. Chem. Res. **12**, 276 (1979).
[71] R. Messmer, D. Salahub, K. Johnson, and C. Y. Yang, Chem. Phys. Lett. **51**, 84 (1977).
[72] H. Y. Jeong, S. K. Kim, J. Y. Lee, and S.-Y. Choi, J. Electrochem. Soc. **158**, H979 (2011).
[73] P. Yao, H. Wu, B. Gao, J. Tang, Q. Zhang, W. Zhang, J. J. Yang, and H. Qian, Nature (London) **577**, 641 (2020).
[74] V. Milo, C. Zambelli, P. Olivo, E. Pérez, M. K. Mahadevaiah, O. G. Ossorio, C. Wenger, and D. Ielmini, APL Mater. **7**, 081120 (2019).
[75] S.-T. Lee and J.-H. Lee, Front. Neurosci. **14**, 571292 (2020).
[76] K. Kamiya, M. Y. Yang, T. Nagata, S.-G. Park, B. Magyari-Kope, T. Chikyow, K. Yamada, M. Niwa, Y. Nishi, and K. Shiraishi, Phys. Rev. B **87**, 155201 (2013).
[77] S.-G. Park, B. Magyari-Kope, and Y. Nishi, IEEE Electron Device Lett. **32**, 197 (2011).
[78] K. Kamiya, M. Young Yang, S.-G. Park, B. Magyari-Köpe, Y. Nishi, M. Niwa, and K. Shiraishi, Appl. Phys. Lett. **100**, 073502 (2012).
[79] G. Henkelman and H. Jónsson, J. Chem. Phys. **113**, 9978 (2000).
[80] G. Henkelman, B. P. Uberuaga, and H. Jónsson, J. Chem. Phys. **113**, 9901 (2000).
[81] R. Nakamura, T. Toda, S. Tsukui, M. Tane, M. Ishimaru, T. Suzuki, and H. Nakajima, J. Appl. Phys. **116**, 033504 (2014).
[82] M. Choi, A. Janotti, and C. G. Van de Walle, J. Appl. Phys. **113**, 044501 (2013).
[83] T. Perevalov, V. Gritsenko, and V. Kaichev, Eur. Phys. J. Appl. Phys. **52**, 30501 (2010).